

Analysis of Morphing Trailing Edge (MTE) Design Configurations

Buckner, Samuel; Johnson, Adam; Yen, Mark

Section 12604 2019-12-05

Abstract—The objective of this experiment was to measure lift-to-drag ratios of a conventional NACA0012 with a hinged aileron and a modified NACA0012 with a Morphing Trailing Edge (MTE) contour at different angles of attack and different trailing edge deflections. The results were then compared to each other to determine whether or not the MTE design produced significant increases in L/D ratios. In order to adequately draw conclusions based on this experiment, knowledge of the design, fabrication, and implementation of MTE airfoil configurations is needed. Also, due to the size of the model fabricated for this experiment, wind tunnel blockage corrections were implemented to further the accuracy of the results. The results of this experiment showed that at a Reynolds number of 247400 ± 9000 and angle-of-attack test matrix of $-10 \pm 1^\circ \leq \alpha \leq 10 \pm 1^\circ$ at 4° increments, a higher L/D ratio occurred for the MTE airfoil than for the airfoil with a hinged aileron at trailing edge deflections of 10° and 20° . In the 10° case, L/D was greater for the MTE between angles of attack of $-4.5 \pm 1^\circ$ and 10° . In the 20° case, L/D was greater for the MTE between angles of attack of $-8 \pm 1^\circ$ and $10 \pm 1^\circ$. These ranges encompass a majority of angles of attack tested, confirming the hypothesis that an MTE increases aerodynamic efficiency on an actuating airfoil. It was also found that the results followed a similar trend to previous research in the case of the 20° trailing edge deflection, helping to confirm the validity and repeatability of previous studies.

Index Terms—Aileron, Morphing Trailing Edge (MTE), Lift-to-Drag Ratio, Coefficient of Drag, NACA0012, Wind Tunnel Corrections

I. INTRODUCTION

The objective of this experiment was to determine whether an NACA0012 with a Morphing Trailing Edge (MTE) would have a higher lift-to-drag ratio than a traditional NACA0012 airfoil with a hinged aileron. In addition, the results were compared to a novel study where an MTE was tested over a similar testing matrix to the one used for this experiment. The original study, conducted by Communier, Botez, and Wong [1], was used to analyze the accuracy of the experimental results of this lab and the reproducibility of the results of the original report.

The experiment conducted by Communier, Botez, and Wong used an NACA0012 airfoil with a rib that is able to deform to a given trailing edge deflection due to the slits cut into it (Fig. 1). The deflection of the trailing edge was controlled by an arm mounted to a rotating servo motor as seen in Fig. 2. This device allowed for real-time deformation of the trailing edge which re-

sulted in a trailing edge deflection which can be equalized to that of a traditional hinged aileron for direct comparison.



Fig. 1. Computer model of the deformation that the rib will undergo to produce an MTE deflection [1].

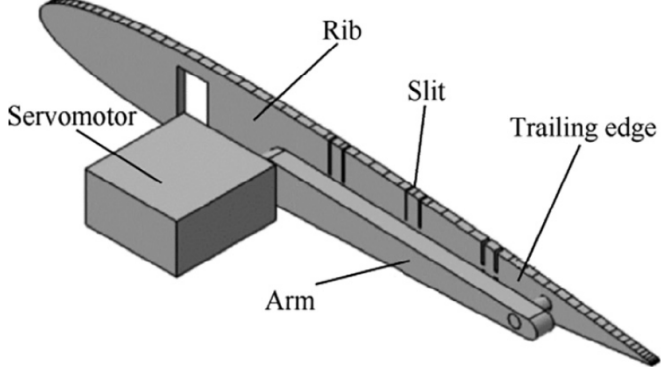


Fig. 2. Servo motor control of the trailing edge rib deformation [1].

The difference between the NACA0012 airfoil with a hinged aileron and the NACA0012 with an MTE deformation can be observed in Fig. 3. Notably, the deflection from the horizontal of the MTE airfoil begins further forward on the chord of the airfoil than where the hinge exists on the aileron airfoil. This aids in the smoothness of the mean camber line (MCL). The theory behind the MTE is that the smoother contour of the MTE compared to a traditional hinged aileron will produce lower values of drag for a roughly-equivalent lift, thereby producing a greater lift-to-drag ratio. A visual inspection of Fig. 3 gives a surface-level, intuitive understanding of why this occurs.

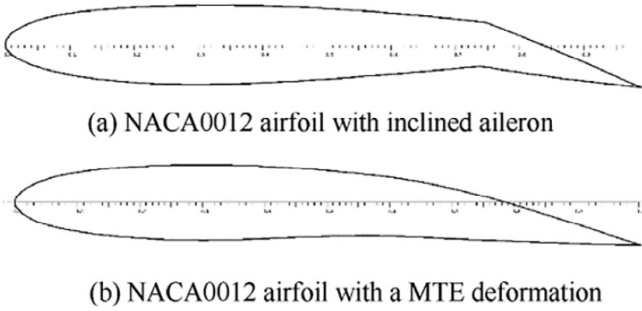


Fig. 3. The difference between the aileron and the MTE is the curvature of the surface of the airfoil [1].

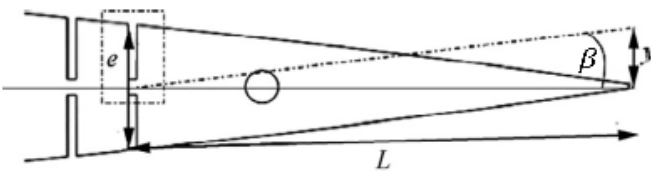
The dimensions of the slits were calculated in the aforementioned study to determine the displacement of the trailing edge. The equations were shown to be:

$$p = \frac{e - t}{2} \quad (1)$$

$$l = p \times \tan \beta \quad (2)$$

$$y = L \times \tan \beta \quad (3)$$

Where p is the depth of the slit, e is the airfoil thickness, t is the thickness between two symmetric slits, l is the width of the slit, β is the angle of the deformation, L is the distance between a slit and the trailing edge, and y is the displacement of the trailing edge. The dimensions of these values can be seen in Fig. 4.



(a) Trailing edge of the rib

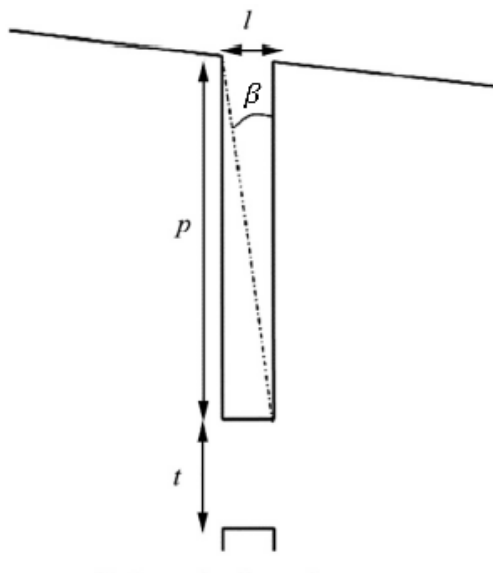


Fig. 4. Calculation of the deformation of the rib [1].

(2) and (3) can be combined to find the direct relationship between the dimensions of the slit to the trailing edge displacement:

$$y = \frac{l \times L}{p} \quad (4)$$

Where y , as seen in Fig. 4(a), is the vertical displacement of the trailing edge from the camber line. And since (4) calculates the displacement from one slit, the total displacement, y_t , from n number of slits in the rib is the summation of the individual displacements, y_i :

$$y_t = \sum_{i=1}^n y_i \quad (5)$$

Substituting (4) into (5) yields:

$$y_t = \sum_{i=1}^n \frac{l_i \times L_i}{p_i} \quad (6)$$

Communier, Botez, and Wong made six slits in their rib, with the dimensions of each slit listed in Table III in the Appendix. This allowed them to achieve a maximum total displacement of 1.33 inches [1].

Since this experiment did not have the budget nor time to manufacture a deformable rib with a servo motor control, an NACA0012 airfoil with three different trailing edge attachments were 3D printed instead. The first attachment was a conventional trailing edge with a hinged aileron. The second attachment mimics the contours of the MTE when β is equal to 10° and the third attachment mimics the MTE when β is 20° . The process of designing the attachments are detailed in the procedures. While these attachments are not precisely MTE devices due to the fact that they cannot morph, they accurately produce the same results an MTE would in the same aerodynamic conditions.

To perform the necessary measurements for the experiment, a two-dimensional dynamometer was used to measure lift and drag forces of each of the airfoil combinations. Prior to obtaining these values, basic values of the wind tunnel flow were obtained. The first flow property obtained was viscosity, which is calculated as follows:

$$\mu_{atm} = \mu_o \left(\frac{0.555T_o + c}{0.555T + c} \right) \left(\frac{T}{T_o} \right)^{\frac{3}{2}} \quad (7)$$

Where T_o is the reference temperature constant of air at 524.07°R , μ_o is the reference viscosity at 0.01827 centipoise, and c is the Sutherland's constant of 120 [2]. It is important to note that the temperature must first be converted to Rankine. In addition, the output for viscosity is in units of centipoise, which must be converted back to $\text{Pa}\cdot\text{s}$ [2].

Another gas property, atmospheric density, can be found using the ideal-gas equation with gas constant $R = 287 \text{ J/kgK}$:

$$\rho_{atm} = \frac{P_{atm}}{RT_{atm}} \quad (8)$$

Where P_{atm} and T_{atm} are the atmospheric pressure and temperature respectively [2].

Furthermore, the relationship between static pressure and dynamic pressure was needed because static pressure was measured at the test section wall. This relationship is governed by:

$$q_\infty = \frac{1}{1-K} (P_{TS} - P_{atm}) \quad (9)$$

Where q_∞ is the free-stream dynamic pressure in the test section, P_{TS} is the static pressure at the test-section wall, P_{atm} is the outside atmospheric pressure, and k is the correlation constant of $-0.4409 \pm 2 \times 10^{-4}$ [3].

Afterwards, the following equation was used to calculate free-stream velocity based on the calculated dynamic pressure:

$$U_\infty = \sqrt{\frac{2q_\infty}{\rho_{atm}}} \quad (10)$$

Where U_∞ is the free-stream flow velocity [4].

Finally, the Reynolds number can be calculated for the airfoil:

$$Re_\infty = \frac{\rho_{atm} U_\infty c}{\mu_{atm}} \quad (11)$$

Where c is the characteristic length [2], which in this case is the chord length of the airfoil.

Once freestream properties and lift and drag forces have been found, the lift and drag coefficients can be calculated with the following, respectively:

$$C_L = \frac{L}{q_\infty S} \quad (12)$$

$$C_D = \frac{D}{q_\infty S} \quad (13)$$

Where L and D are lift and drag forces, respectively, and S is the platform area of the airfoil.

An issue experienced during wind tunnel testing is the wall effects, especially on a relatively large model such as the one used in this lab. A full-scale aircraft in flight does not feel wall effects because many aerodynamic phenomena, such as flow separation, will dissipate into the atmosphere. Since the values obtained from (12) and (13) do not take into account wind tunnel wall effects, they are considered "uncorrected" results. Therefore, to make the necessary blockage corrections, the total velocity increment, ϵ , must be calculated:

$$\epsilon = \epsilon_{sb} + \epsilon_{wb} \quad (14)$$

ϵ_{sb} is the contribution due to solid blockage and is calculated as:

$$\epsilon_{sb} = \Lambda \sigma \quad (15)$$

Where Λ is the body shape factor for an NACA0012 obtained from Fig. 5, and:

$$\sigma = \frac{\pi^2}{48} \left(\frac{c}{h} \right)^2 \quad (16)$$

where c is the chord length and h is the wind tunnel height.

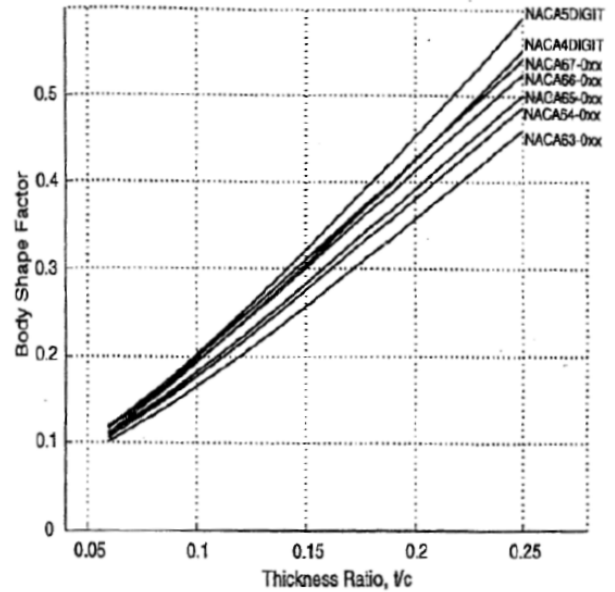


Fig. 5. The value of Λ based on airfoil configuration and thickness ratio [5].

ϵ_{wb} is the contribution due to wake blockage and is calculated as:

$$\epsilon_{wb} = \frac{c}{2h} C_{Du} \quad (17)$$

Where C_{Du} is the uncorrected coefficient of drag obtained from (13). Notice that the correction factor increases as the angle of attack increases. This is because wake blockage increases as α increases.

After finding the correction factors, the corrected values for velocity, freestream dynamic pressure, Reynolds number, angle of attack, coefficient of lift, and coefficient of drag at zero angle of attack are, respectively:

$$U = U_u (1 + \epsilon) \quad (18)$$

$$q = q_u (1 + 2\epsilon) \quad (19)$$

$$Re = Re_u (1 + \epsilon) \quad (20)$$

$$\alpha = \alpha_u + \frac{57.3\sigma}{2\pi} (C_{Lu} + 4C_{M\frac{1}{4}u}) \quad (21)$$

$$C_L = C_{Lu} (1 - \sigma - 2\epsilon) \quad (22)$$

$$C_{D0} = C_{D0u} (1 - 3\epsilon_{sb} - 2\epsilon_{wb}) \quad (23)$$

Where variables with the u subscript are values that have not been corrected. For further clarification, U_u is the value from (10), q_u is from (9), Re_u is from (11), α_u is the measured angle of attack, C_{Lu} is from (12), C_{D0u} is from (13) at zero angle of attack, and $C_{M\frac{1}{4}u}$ is directly calculable using values of lift and drag applied at the dynamometer mounting location (however will not be used for further analysis).

The results of this experiment showed that at a Reynolds number of 247400 ± 9000 , a higher L/D ratio occurred for the MTE airfoil than for the airfoil with a hinged aileron at trailing edge deflections of 10° and 20° . In the 10° case, L/D was greater

for the MTE between angles of attack of $-4.5 \pm 1^\circ$ and 10° . In the 20° case, L/D was greater for the MTE between angles of attack of $-8 \pm 1^\circ$ and $10 \pm 1^\circ$. These ranges encompass a majority of angles of attack tested, confirming the hypothesis that an MTE increases aerodynamic efficiency on an actuating airfoil. It was also found that the results followed a similar trend to the previous research in the case of the 20° trailing edge deflection [1].

II. PROCEDURE

Airfoil, MTE, and Aileron Design and Fabrication

The first step to designing the MTEs was to develop an in-house MATLAB image-processing algorithm that takes the airfoils from Fig. 3 and constructs evenly-spaced data-points along their contours. These airfoils correspond to an angular deflection of $\beta = 14.4^\circ$. Of particular importance is the MTE-deformed airfoil, which will be used as the basis for building the MTE configurations used in this lab.

A secondary in-house MATLAB algorithm is applied to linearly "stretch" the MTE-deformed end of the original 14.4° MTE to a new trailing-edge deformation, which corresponds to, in the case of this experiment, 10° and 20° . These stretch deformations increase along the aft-half of the airfoil, however thickness of the airfoil along the mean camber line is kept constant to closely mimic the effects of slit deformations performed previously [1]. These new MTE designs, along with their corresponding aileron designs, can be seen in Fig. 6 and Fig. 7 (note, in these plots, that deflection angle θ refers to the same quantity as β).

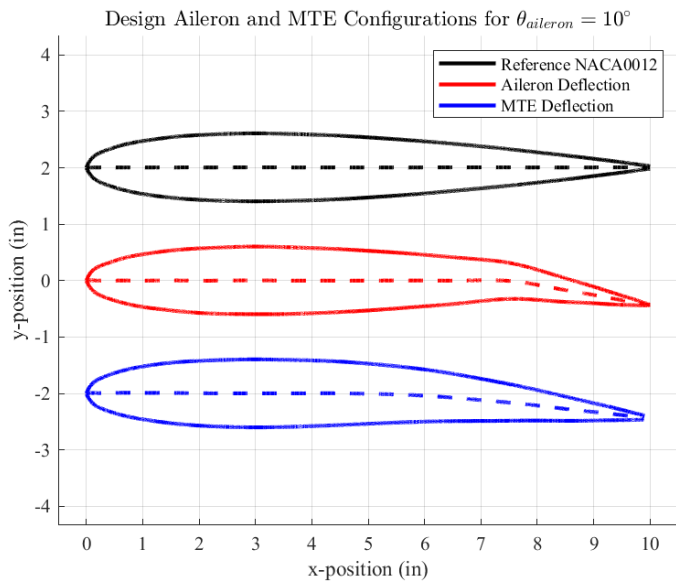


Fig. 6. MATLAB comparison between the airfoil with 0° deflection, 10° discontinuous deflection, and 10° continuous deflection.

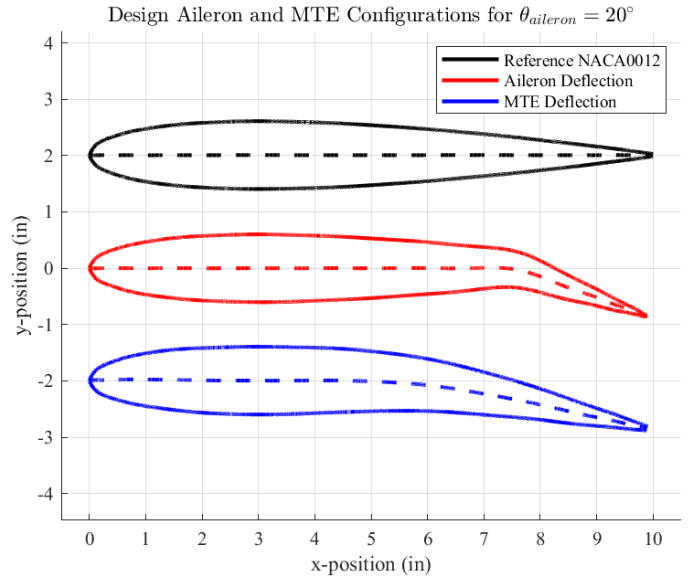


Fig. 7. MATLAB comparison between the airfoil with 0° deflection, 20° discontinuous deflection, and 20° continuous deflection.

Afterwards, SolidWorks was used to construct the MATLAB-generated MTE airfoils using the spline tool with imported data-points. Rather than produce three separate models, a single fixed body was designed with three trailing edge attachments. The main body is the fixed portion of the airfoil and is 6 in long, spans the width of the wind tunnel test section at 11.9 in long, and has a curved end with two slots for a bracket that fastens to the trailing edge attachments (Fig. 8). The main body also has a threaded rod that protrudes from the leading edge when secured to connect to the dynamometer. This is because the dynamometer is located towards the front of the test section, so the model must be located behind the instrument. The threaded rod threads into an OTS friction hinge which is then fastened to the internal of the airfoil. This hinge allows for a sturdy adjustment of the angle of attack of the airfoil. The three attachments (Fig. 9) consists of a traditional aileron that can be deflected to 10° and 20° , a 10° MTE deflection, and a 20° MTE deflection.



Fig. 8. The fixed body of the NACA0012 airfoil with the threaded rod and hinge fastened to it.

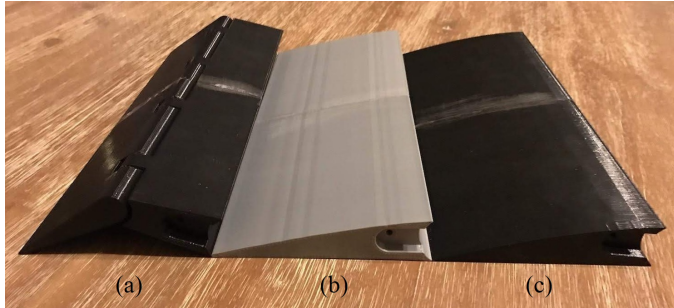


Fig. 9. Traditional aileron attachment (a), 10° MTE deflection (b), 20° MTE deflection (c).

Experimental Procedures

Prior to running the experiment, the lift and drag components of the dynamometer were calibrated with an MKS Baratron series 200 (model no. 223B-22875) transducer to set the zero and span of each of the two dimensions independently of one another. The atmospheric temperature and pressure were recorded throughout the experiment and were used to calculate atmospheric viscosity and density using (7) and (8), respectively. Afterwards, the wind tunnel, ELD Model 402, was run and the static pressure at the wall was measured, which was used to calculate dynamic pressure and free-stream velocity using (9) and (10), respectively; this corresponded to a free-stream velocity of 15.3 ± 0.6 m/s. Finally, the Reynolds number of the flow can be calculated using (11).

The airfoil body was first connected to an aileron attachment to mimic a conventional NACA0012 airfoil with a hinged aileron. The aileron was deflected and fixed to 10° using a specialized brace at the center-span, and the body was attached to the dynamometer such that a threaded rod protrudes from the front of the airfoil and connects to the instrument. A side view of the setup can be seen in Fig. 10.

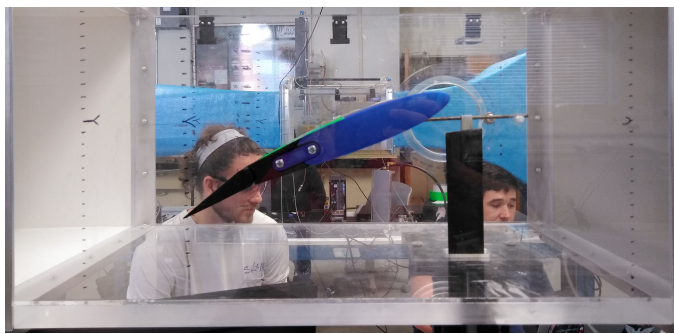


Fig. 10. Side view of the airfoil connecting to the dynamometer.

From the top view, seen in Fig. 11, it is shown that the panel to access the inside of the airfoil is sealed with low-friction tape to reduce the aerodynamic drag effects of protrusions caused by the panel on the airfoil.

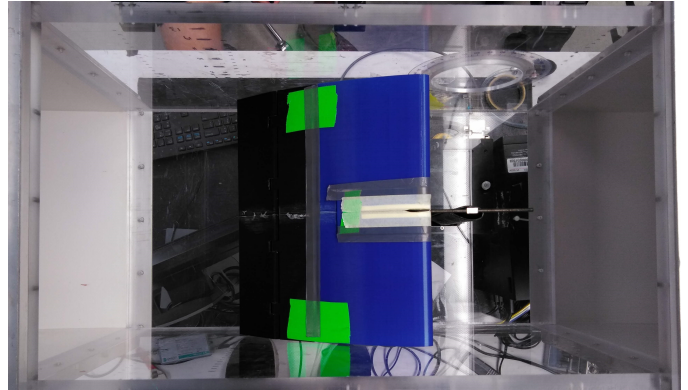


Fig. 11. Top view of the airfoil setup.

And from the front view in Fig. 12, it can be seen that a deformable envelope formed with a combination of masking tape and high-rigidity mounting tape was used to cover the slot where the threaded rod protrudes from to reduce the effects of aerodynamic drag force on the cavity while still allowing for the actuation of the internal friction hinge. It can be observed that tape was used in multiple other areas as well - it was reasoned that the addition of tape to smoothen out an unwanted opening (which exist merely due to necessary 3D printing tolerances) would provide improved accuracy as opposed to not including it at all.

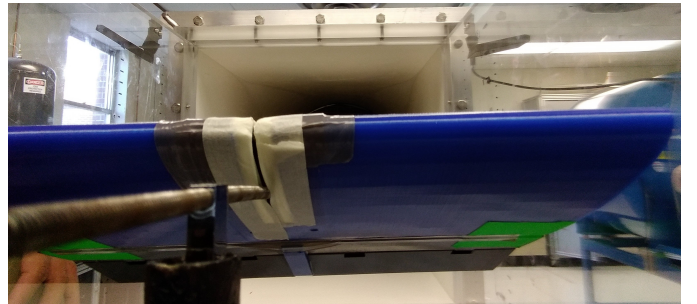


Fig. 12. Front view of the airfoil setup.

To begin the lift and drag data acquisition phase of the experiment, the airfoil was set to $0 \pm 1^\circ \alpha$ and 0° aileron deflection. Lift and drag values were then recorded multiple times. Next, the aileron deflection was adjusted to 10°. Using the friction hinge fastened inside the airfoil, the angle of attack was adjusted from $-10 \pm 1^\circ$ to $10 \pm 1^\circ$ at $4 \pm 1^\circ$ increments, measured using a protractor; the lift and drag values were recorded from the dynamometer at each α multiple times. This process was repeated for an aileron deflection of 20°.

Next, the same measurements from $-10 \pm 1^\circ$ to $10 \pm 1^\circ$ at $4 \pm 1^\circ$ increments were taken for an MTE attachment of 10° deflection as seen in Fig. 13 and for an MTE attachment of 20° deflection as seen in Fig. 14.



Fig. 13. Mounted airfoil with 10° deflection MTE attachment.

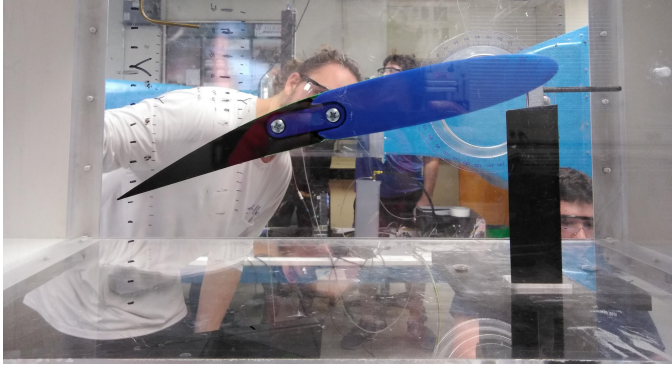
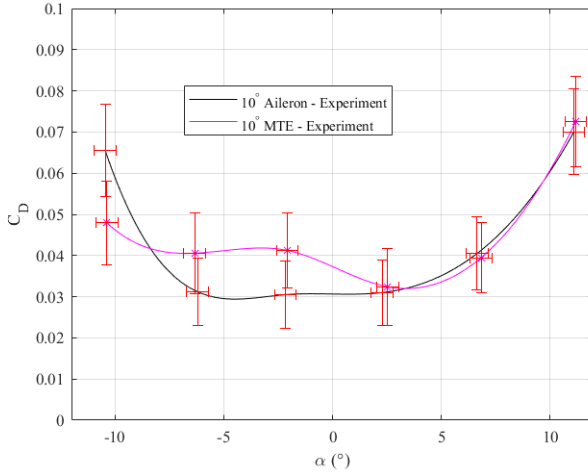


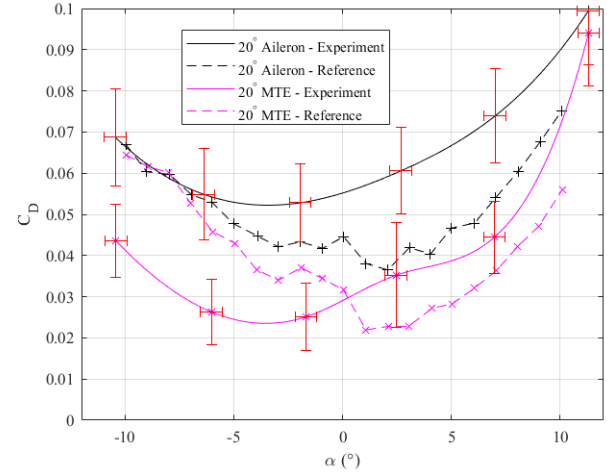
Fig. 14. Mounted airfoil with 20° deflection MTE attachment.

III. RESULTS

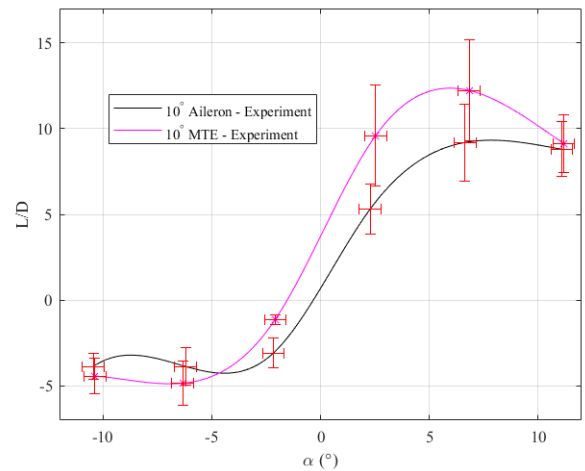
When looking solely at C_D vs. α for the 10° aileron deflection and MTE deflection (Fig. 15), the MTE had a higher drag coefficient from an α of $-8 \pm 1^\circ$ to $3 \pm 1^\circ$. Then, as angle of attack increased, both drag coefficients were approximately equal to each other. Error bars are shown in both the α and C_D direction to represent uncertainty in the calculations. Note that curve-fits are applied between data-points strictly for visualization

Fig. 15. C_D vs. α for 10° MTE and aileron deflection.

When looking solely at C_D vs. α for the 20° aileron deflection and MTE deflection (Fig. 16), a different phenomenon occurs. The aileron had a higher drag coefficient throughout the range of the tested angles of attack before approaching convergence with the MTE at $10 \pm 1^\circ$ angle of attack. Also noteworthy is the addition of reference data from [1]. A MATLAB script was developed to extract data from reference plots and compile them into the same graph for direct unfiltered comparison.

Fig. 16. C_D vs. α for 20° MTE and aileron deflection.

When looking at L/D ratios for the 10° aileron and MTE deflections (Fig. 17), it is apparent that the ratio produced by the MTE is greater from an α of $-4.5 \pm 1^\circ$ to $10 \pm 1^\circ$. However, the aileron produced a higher ratio from an α of $-4.5 \pm 1^\circ$ to $-10 \pm 1^\circ$. Both the MTE and the aileron converged at angles of attack of $-10 \pm 1^\circ$, $-4.5 \pm 1^\circ$, and $10 \pm 1^\circ$.

Fig. 17. L/D vs. α for 10° MTE and aileron deflection.

The L/D ratios for the 20° aileron and MTE deflections as well as the results from [1], used as a reference, are shown in Fig. 18. The MTE L/D is greater from an α of $-8 \pm 1^\circ$ to

$10 \pm 1^\circ$. The aileron's L/D was greater from an α of $-8 \pm 1^\circ$ to $-10 \pm 1^\circ$. Notably, the error bars for the aileron are recognizably smaller than those for the MTE at most mean data points.

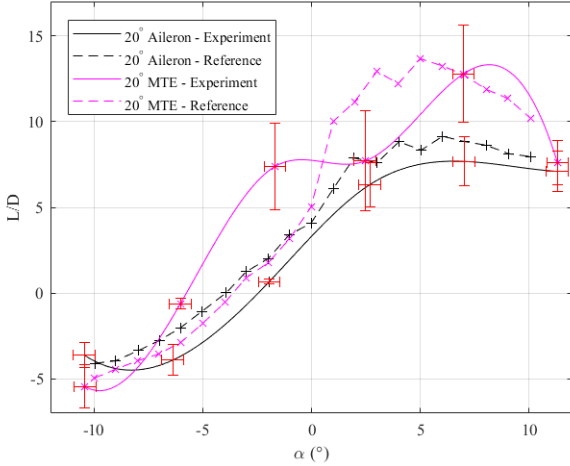


Fig. 18. L/D vs. α for 20° MTE and aileron deflection.

TABLE I.
Laboratory Results and Measurements

Symbol	Quantity	Value
Re_U	Uncorrected Reynolds number	247000 ± 9000
V_U	Uncorrected Velocity	15.3 ± 0.4 m/s
T_{atm}	Atmospheric Temperature	297.3 ± 0.2 K
P_{atm}	Atmospheric Pressure	101400 ± 30 Pa
ρ_{atm}	Atmospheric Density	1.184 ± 0.001 kg/m ³
μ_{atm}	Atmospheric Viscosity	$1.859 \times 10^{-5} \pm 5 \times 10^{-9}$ Pa·s

TABLE II.
Geometric Measurements of Airfoils and Test Section

Symbol	Quantity	Value
c	Chord Length	0.2540 ± 0.0005 m
e	Airfoil Thickness	0.0305 ± 0.0005 m
b_{wing}	Airfoil Span	0.3023 ± 0.0005 m
h	Wind Tunnel Height	0.3048 ± 0.0005 m
w_{tunnel}	Wind Tunnel Width	0.3048 ± 0.0005 m

IV. DISCUSSION

Data Comparisons

Several conclusions and inferences can be made based on the results gathered and compiled. First, with regards to the data for the 10° trailing edge deflections, it should be noted that reference data was not available for comparison. It was determined that repeating the experiment at more than one trailing edge deflection would serve as a verification of the repeatability and reproducibility of the experimental method developed for this lab. The confirmation of this is especially prevalent in the similarities of the L/D curves for both trailing edge deflection angles (Fig. 17 and Fig. 18).

It can be difficult to draw conclusions from some points in the graphs due to the large error bars, implying that the curves could be drastically different. The large error bars could imply

a number of issues during experimentation. For example, due to the difficult problem of mounting a relatively heavy model in the wind tunnel such that it is essentially suspended in free space but also spans the whole width of the test section, there was notable fluttering of the airfoil that could have influenced the lift and drag data and produced higher variability between the data points.

As previously mentioned, the 10° trailing edge deflection data was generated to be a comparison between the experimental data from the 20° trailing edge deflection portion of the experiment. In some ways, the comparison verified the experiment, in other ways, significant differences arose. The similarities in the L/D curves between the two trailing edge deflections was already mentioned. However, there are notable differences between the two C_D curves. The drag was significantly lower at almost all angles of attack in the case of the 20° MTE with respect to the 20° aileron. However, in the 10° case, the MTE and aileron's drag were much closer, and for a large range of angles of attack, the MTE had higher drag. This could have been an experimental anomaly that could have arisen from a myriad of factors. As one example, if the friction hinge was not tightened adequately, the angle of attack could have changed slightly when there was flow in the test section.

When comparing the 20° experimental data to the reference data, the most interesting note is that at most values of α , the reference curves had notably less drag than their experimental counterparts. This is likely due to the fact that the experimenters who developed the reference data had more resources at their disposal allowing them to construct more streamlined airfoils and experimental methods that generate less drag. This fact is not present in the L/D curve, however, which implies that the airfoil used in this experiment made up for its greater drag in comparison to the reference data with proportionally greater lift, resulting in a more closely-fitted lift-to-drag curve.

Most importantly, the results suggest that the MTE does have a significant L/D advantage over the hinged aileron. As mentioned in the results, the L/D is higher for the MTE over the majority of angles of attack tested in both deflection cases. Notably, in both cases, the greatest difference in L/D , so the greatest gain in aerodynamic efficiency, occurred between $5 \pm 1^\circ$ and $10 \pm 1^\circ$ angle of attack. This is especially useful for a symmetric airfoil such as the NACA0012 which can stall in the same range of angles of attack. With a greater L/D provided by the MTE, stall could be prevented or delayed.

Applications to Low-Speed Aircraft

The applications noted in the reference paper suggested use by drones or unmanned aerial vehicles (UAVs) due to their irregular flight paths [1]. The efficiency gains from an MTE over a traditional hinged aileron could result in significantly lower fuel consumption in low-speed, quick-maneuvering aircraft such as low-altitude UAVs. An application specific to this experiment could be that of an MTE on an NACA0012 airfoil used as a vertical stabilizer and rudder. The NACA0012 airfoil sees common application as an aircraft or even watercraft rudder. In this case, the lesser drag experienced by an MTE in comparison to a hinged aileron could be beneficial in an application as a rudder.

Notes on Manufacturing

An important consideration in the real-world application of the MTE to aircraft is that of the manufacturing engineering and materials engineering difficulties in the production of the devices. The model for this lab proved to be rather difficult to design and fabricate and it is a static model that doesn't deform or morph. It might be determined that the research and development costs of developing a sound manufacturing process for an MTE wing would outweigh the cost savings of the drag reduction from the application of the MTE. It is also possible however, that there exists an elegant solution to the manufacturing problem, in which case MTEs may see wide-spread applications in aircraft of the future.

V. CONCLUSION

The key findings of this experiment involved calculating lift-to-drag ratios of a conventional NACA0012 airfoil with a hinged aileron and a modified NACA0012 with an MTE. These values were compared to each other to determine that an airfoil with an MTE had higher L/D ratios in comparison to a traditional hinged aileron over a majority of angles of attack tested. The results were compared to the study conducted by Communier, Botez, and Wong to further verify the findings, where the reproducibility of that experiment was confirmed. The importance of these results is that as technology continues to advance, wings can be designed to morph their trailing edges under different flow conditions so that the aircraft can always operate at the highest aerodynamic efficiency. It is recommended for future studies to measure lift and drag forces at smaller α increments to improve the accuracy of the L/D ratio at each angle of attack, as well as to work on improvement of various mechanical issues mentioned previously (induced wing flutter, smoothened wing surface, etc.)

APPENDIX

TABLE III.
Dimensions of Slits in Rib

Slit number	l_i [in]	L_i [in]	p_i [in]
1	0.026	4.911	0.416
2	0.026	4.635	0.4
3	0.021	3.609	0.34
4	0.021	3.338	0.317
5	0.014	2.317	0.233
6	0.014	2.053	0.205

Uncertainty Analysis

An in-depth investigation on the uncertainty for each component described in the results was conducted to help validate the results. Uncertainty can generally be decomposed into two components: precision error (tendency of a data-set to deviate from the mean) and bias error (offset of a data-set's mean from a desired output). Precision error for a data-set will be calculated as follows:

$$P_X = \frac{S}{\sqrt{N}} \quad (24)$$

Where S refers to the standard deviation and N refers to the number of data points. Bias error, B_X , corollary to accuracy, is found in the accuracy error of the measurement apparatus (Table IV). As a quick note for Table IV, the pressure transducer contains two components of accuracy error, one for raw accuracy error of 1% and one for accuracy error in the manometer calibration of 12.44 Pa. All of these bias errors will be used to propagate uncertainty further down the line into other values.

TABLE IV.
Measurement Accuracy Errors

Measurement	Apparatus	Accuracy Error
T_∞	Temperature Scale	0.05 K
P_∞	Vernier Scale	0.05 mmHg
e	Calipers	0.05 mm
c, h	Ruler	0.05 cm
w_{tunnel}	Ruler	0.05 cm
b_{wing}	Ruler	0.05 cm
L, D	Dynamometer	0.0255 N
$P_{TS} - P_{atm}$	Pressure Transducer	$0.01(P_{TS} - P_{atm}) + 12.44$ Pa

As a quick note, the dynamometer uncertainty is variable based on the magnitude of the measurement with a maximum of 0.0255 N, calculated using the weights used in the calibration curve (where the bias error is represented as the difference between design and scale-measured weight). The bias error used is based on the bias error of the next-highest calibration point as a safe slight overshoot of the bias error. Finally, these precision and bias errors can be then used to calculate the uncertainty of the variable in question, X , using:

$$\mu_X = \sqrt{B_X^2 + (T_{v,95}P_X)^2} \quad (25)$$

Where $T_{v,95}$ refers to the T-distribution value at a 95% confidence interval for v degrees of freedom ($v = N - 1$) and N is the number of data points.

Next, the propagation of uncertainty through consequent calculations using the previous measurements must be discussed. For a desired value X which must be calculated through an equation of N independent variables θ_N , precision and bias errors for X can be calculated using the root-square-sum (RSS) method as follows:

$$P_X = \sqrt{\left(\frac{\partial X}{\partial \theta_1} P_{\theta_1}\right)^2 + \dots + \left(\frac{\partial X}{\partial \theta_N} P_{\theta_N}\right)^2} \quad (26)$$

$$B_X = \sqrt{\left(\frac{\partial X}{\partial \theta_1} B_{\theta_1}\right)^2 + \dots + \left(\frac{\partial X}{\partial \theta_N} B_{\theta_N}\right)^2} \quad (27)$$

As an example, for (8), the desired variable $X = \rho_{atm}$, the independent variables are $\theta_1 = P_{atm}$ and $\theta_2 = T_{atm}$, and the constant is R which is accounted for only in the partial derivatives.

Furthermore, the number of degrees of freedom, v , for X can be calculated using the Welch-Satterthwaite method:

$$v_X = \frac{\left(\sum_{i=1}^N \left[\frac{\partial X}{\partial \theta_i} P_{\theta_i}\right]^2\right)^2}{\left(\sum_{i=1}^N \left[\frac{\partial X}{\partial \theta_i} P_{\theta_i}\right]^4 / v_{\theta_i}\right)} \quad (28)$$

Finally, all components have been calculated for desired variable X that are required to make use of (25) to calculate μ_X . This approach allows the capability to calculate uncertainties for all desired variables from (7) to (23).

REFERENCES

- [1] D. Communier, R. Botez, and T. Wong, “Experimental validation of a new morphing trailing edge system using Price Paidoussis wind tunnel tests,” *Chinese Journal of Aeronautics*, vol. 32, 6.
- [2] S. Buckner, A. Johnson, and M. Yen, “Coefficient of Pressure Over a Cylinder and Calculation of Drag Coefficient at a Specified Reynolds Number,” *EAS4810C-Aerospace Sciences Lab and Design*, 2019.
- [3] ——, “EAS4810C - Laboratory 1,” *EAS4810C-Aerospace Sciences Lab and Design*, 2019.
- [4] ——, “Velocity Spectra and Profile of a Cylinder using a Hot Wire Anemometer,” *EAS4810C-Aerospace Sciences Lab and Design*, 2019.
- [5] J. Abbitt and L. Ukeiley, “Lab 5 Revision 10-16-2019,” *EAS4810C Aerospace Sciences Lab and Design*, 2019.